Accepted for presentation in: 2022 IEEE Future Networks World Forum (FNWF), Montreal, Canada, October 2022.

3D Self-Motion Tracking Services: Coalescence of mmWave Beam Orientations and Phase Information

Simon Häger, Stefan Böcker, and Christian Wietfeld
Communication Networks Institute (CNI), TU Dortmund University, 44227 Dortmund, Germany
E-mail: {Simon.Haeger, Stefan.Boecker, Christian.Wietfeld}@tu-dortmund.de

***Abstract*—The profound integration of sensing functionalities is seen as a major step stone towards unleashing the full potential of 6G, yet recent advances in current networks already offer new opportunities for sensing. This is especially true for the mmWave domain which offers a suitable environment for sensing services, e.g. due to the ability to detect and determine the angles of available link opportunities. Whereas previous work devised a fine 3D motion tracking by combining phase measurements along with several co-deployed nodes' links to the mmWave network, this work instead exploits multiple available propagation paths. We observe sub-10 µm 3D motion tracking accuracy for the proposed single user equipment (UE) enhancement, mirroring the conventional multi-UE-based approach performance. However, our detailed error analysis finds that multipath may turn from friend to foe if undesired components are not suppressed sufficiently, as these amplify the effects of phase distortions due to channel noise and hardware imperfections. Our evaluation further yields that the technique is sensitive to erroneous propagation path angle information.**

I. Introduction

Due to similarities between wireless communications and radar transceiver architectures, and the insight that any signal with sufficient strength may be exploited, the notion of joint communication and radio/radar sensing (JCAS) has emerged as a key topic of preliminary 6G discussions [1]. Another driving force for JCAS is the transition to the mmWave spectrum, which offers wide frequency bands, the ability to orient highly-directional antenna beams electronically as needed, and low multipath [2], [3]. While there have already been several exciting practical works, a wide range of hardware and signal processing-related issues must still be solved within the next decade. Conversely, we find that research on innovative *channel-as-a-sensor*-based services leveraging current mobile network technology is neglected. This is at a bad timing now that 5G mmWave modems and antennas are gaining traction.

Radio channel-based sensing has been studied extensively for various sub-6 GHz deployments, e.g. for vehicular traffic detection and classification [4]. It was shown in [5] that mmWave cellular network infrastructure can be leveraged similarly to detect and track fine-grained 3D motions which are, for example, being induced on fixed wireless access (FWA) UEs during earthquakes or by heavy traffic, cf. Fig. 1a. It was found that millimeter range movements can be reconstructed with sub-10 µm 3D error by jointly exploiting phase measurements of reference signals and pencil beam orientations known from beam management. For this purpose, phase and orientation information of several close-by mounted UEs' Line-of-Sight (LOS) paths to the network was fused. However, the need for several UEs is impractical. Instead, in this work we show that a single UE suffices when exploiting several distinct available spatial link opportunities as illustrated in Fig. 1b. The enhancement is based on the following two aspects: First, that phase measurements can only detect movement along the dominant incident wave axis, and second, that mmWave beam patterns allow for deliberate targeting of any distinct propagation path while suppressing others. In that case, our proposed enhancement describes a mmWave-specific carrier phase difference of arrival (CPDoA) technique in the scope of future cellular positioning [6] which is of particular interest for industrial campus networks. Using mounted cellular modems to connect machines reliably to the private network, the single UE may now further measure machine vibrations to assess the internal states [7] as a secondary use. Thus, a detailed performance under effects encountered in practice is required. This work therefore studies the applicability of the proposed enhancement and further investigates the performance under sources of error such as beam misalignments.

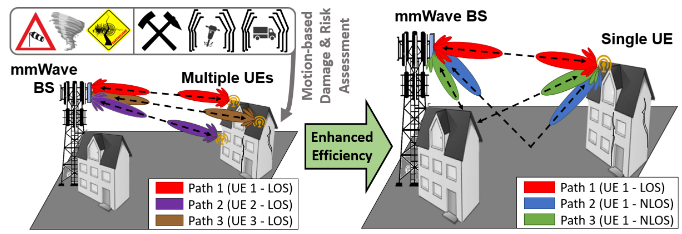

(a) Multi-UE link monitoring of induced motions. (b) Single UE exploiting link and reflections.

Fig. 1. *(a)* Alternative approach investigated in [5] provides infrastructure monitoring services via links of several UEs. *(b)* Practical enhancement: Deliberate use of distinct spatial link opportunities of a single UE to measure its own motion in 3D space.

The rest of the paper is organized as follows: In Sec. II we enhance the mmWave microscopic 3D motion sensing (M^3S) measuring technique and discuss practical sources of error. We then introduce our evaluation methodology in Sec. III and discuss the results in Sec. IV.

II. Related Work

A. Multipath-Enabled M^3S Technique

The number of available, distinct link opportunities U between base station (BS) and UE can be determined easily after initial access during which a beam training protocol such as exhaustive search measures all pencil beam combinations to select the one which maximizes throughput [8]. Due to this procedure, beam orientation information may be derived for all

U paths. Additional beam management procedures and the use of angle-finding algorithms, e.g. [9], allow for refinement of the beams for each detected path such that the optimal azimuth and elevation beam orientations (ϕ_u, θ_u), $u = 1, \ldots, U$, are determined. In practice, up to five paths are expected [3], [10].

The second key component of M^{3}S consists of measuring phase information per propagation path as comprised within the channel estimate vector $\overrightarrow{h_u}(f)$ for time instances t, which is available at N subcarriers $f_n = f_0 + n \cdot \Delta f$, $n = 0, 1, \ldots, N-1$ acquired at a rate $1/\Delta t$. Once the UE moves by $\overrightarrow{m_{\text{move}}} \in \mathbb{R}^{3\times 1}$, phase changes $\overrightarrow{\delta_u}(f) = \overrightarrow{h_u}|_{t=t_{u,1}} - \overrightarrow{h_u}|_{t=t_{u,0}} \in (-180, 180]^\circ$ occur, where $t_{u,1} = t_{u,0} + \Delta t$. After unwrapping the phase change vector, the movement magnitude $\widehat{d_u}$ along propagation path u can be estimated, cf. Eq. 1 using speed of light c_0.

$$\widehat{d_u} = \underset{n=0,\ldots,N-1}{\text{mean}} \left\{ \frac{\text{unwrap}\{\overrightarrow{\delta_u}\}|_{f=f_n}}{180^\circ} \cdot \frac{c_0}{f_n} \right\} \tag{1}$$

The estimates $\widehat{d_u}$ differ as they are along the U distinct identified incident wave axes $\overrightarrow{r_u}(\phi_u, \theta_u) \in \mathbb{R}^{3\times 1}$. With the aid of the two mutually orthonormal vectors $\overrightarrow{e_{A,u}}$, $\overrightarrow{e_{B,u}} \perp \overrightarrow{r_u}$, the linear equation system $\overrightarrow{b} = A \cdot \overrightarrow{c}$ is set up with vector $\overrightarrow{b} \in \mathbb{R}^{3(U-1)\times 1}$ and matrix $A \in \mathbb{R}^{3(U-1)\times 2U}$ as follows:

$$\overrightarrow{b} = \begin{pmatrix} \widehat{d_2} \cdot \overrightarrow{r_2} - \widehat{d_1} \cdot \overrightarrow{r_1} \\ \widehat{d_3} \cdot \overrightarrow{r_3} - \widehat{d_1} \cdot \overrightarrow{r_1} \end{pmatrix} \tag{2}$$

$$A = \begin{pmatrix} \overrightarrow{e_{A,1}}, & \overrightarrow{e_{B,1}}, & -\overrightarrow{e_{A,2}}, & -\overrightarrow{e_{B,2}}, & 0_{3x1}, & 0_{3x1} \\ \overrightarrow{e_{A,1}}, & \overrightarrow{e_{B,1}}, & 0_{3x1}, & 0_{3x1}, & -\overrightarrow{e_{A,3}}, & -\overrightarrow{e_{B,3}} \end{pmatrix} \tag{3}$$

Note that there must be at least three propagation paths for an (over)determined system, e.g. Eqs. 2-3 with U=3. Last, the 3D motion is reconstructed using elements $\widehat{c_i} \in \overrightarrow{c}$, $i = 1, \ldots, 2U$:

$$\overrightarrow{m_{\text{meas}}} = \underset{u=1,\ldots,U}{\text{mean}} \left\{ \widehat{d_u} \cdot \overrightarrow{r_u} + \widehat{c}_{2u-1} \cdot \overrightarrow{e_{A,u}} + \widehat{c}_{2u} \cdot \overrightarrow{e_{B,u}} \right\}. \tag{4}$$

B. Degrading Effects on System Performance

Several effects impose measurement error on the proposed M^{3}S technique. As found in [5], one exemplary source of error is related to the *condition number* (CN) $\|A^{-1}\|_2 \cdot \|A\|_2$ of matrix A, cf. Eq. 3, particularly when the radio environment only allows for three propagation paths. If the beam orientations for these link opportunities lead to a near-singular matrix A, i.e. a large CN, usage of A^{-1} results in a highly unstable solution such that the pseudo-inverse is enforced. CNs may thus be used as a detector for unsuitable path combinations.

The wireless domain is inherently prone to uncertainty because approximately additive white Gaussian noise (AWGN) affects each transmission. Depending on the measured signal-to-noise ratio (SNR), it may be necessary to repeat measurements. This is one of the reasons why estimation of (ϕ_u, θ_u) of the U paths is prone to errors, so-called beam misalignments, which result in the construction of an erroneous matrix A, cf. Eq. 3. There are further practical issues in transceivers that affect phase measurements. Random fluctuations of phase and frequency of the local oscillator (LO) mixer signal are called phase noise (PN), which is particularly strong at mmWave frequencies and rotates the complex data on each subcarrier equally [2]. Similarly, the sampling rate LO introduces a linear increasing phase shift over the subcarriers.

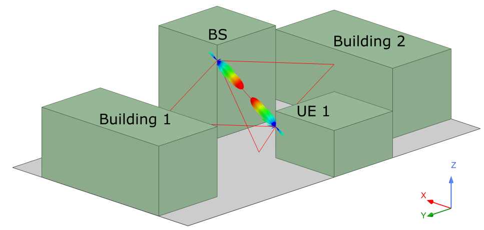

(a) Use of LOS path via well-aligned pencil beams.

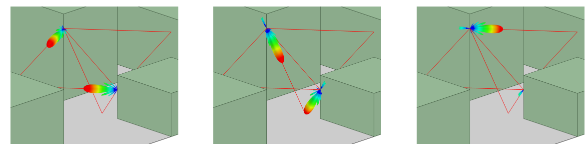

(b) BR1 path. (c) GR path. (d) BR2 path.

Fig. 2. Sample scenario with four distinct link opportunities [– lines] between mmWave BS and mounted UE. *(a)* Payload transmissions are via LOS path. *(b)–(d)* Additional NLOS paths enable single-UE 3D motion tracking.

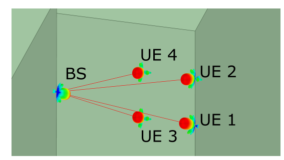

Fig. 3. Considering the same sample environment as in Fig. 2a, the former multi-UE-based approach in [5] employs one path per UE: Beam management capabilities and spatial mmWave channel characteristics are not used to the fullest extend compared to the proposed enhancement.

Moreover, our derivation in Sec. II-A did not discuss the relation between time instances $t_{u,0}$, $u = 1, \ldots, U$. Ideally, all paths are measured at the same time, but this is not possible when using the mmWave-typical analog beamforming (ABF) [2]. The larger the resulting time difference between $t_{1,0}$ and $t_{U,0}$, the more likely there is an additional error due to an ongoing movement process. Scheduling of the required signals is however up to the network operator. Use of lavish hybrid beamforming (HBF) architectures could resolve this by enabling simultaneous facilitation of several beams in contrast to ABFs, yet inter-beam interference may arise in turn.

At last, if hierarchical beam training algorithms are used by the mmWave network instead of exhaustive search [8], fewer link opportunities than available may be detected due to the reduced beamforming gain of sector beams. This, as well as the need for transmit power sharing when using multiple beams, could deteriorate performance [5], or even service availability if U drops below three. A counter measure would be the use of links to several BSs. Considering the prospect of reconfigurable intelligent surfaces (RISs) in future networks, suitable paths could also be provided on demand [11].

III. Methodology

In this section, we first introduce our ray-tracing setup and the implemented scenarios. In Sec. III-B, we then explain the methodology for the verification of the multipath-based approach we have described in Sec. II-A. Last, we introduce how the performance is assessed under specific error sources as discussed in Sec. II-B.

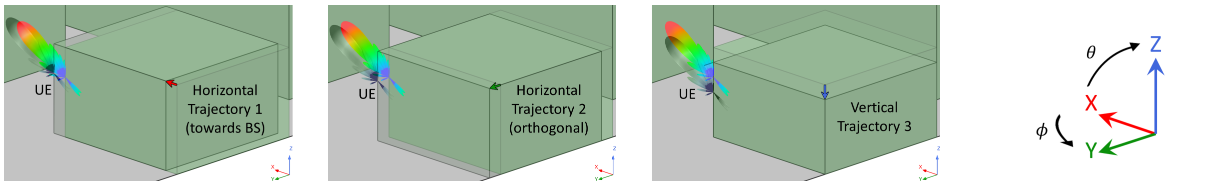

(a) $x_{\text{shift}} = 0, 1, \ldots, 5\,\text{mm}$. (b) $y_{\text{shift}} = 0, 1, \ldots, 5\,\text{mm}$. (c) $z_{\text{shift}} = 0, -1, \ldots, -5\,\text{mm}$. (d) UE coordinate system.

Fig. 4. *(a)–(c)* Baseline scenario (colorized) with considered infrastructure movements (shaded). *(d)* UE-side coordinate system.

A. Simulation Setup & Deployment Scenario

We have first used a commercial electromagnetic (EM) simulation software[1] to design an 8×8 uniform planar array (UPA) which provides 19.79 dBi antenna gain with 13.29° half-power bandwidth (HPBW) at boresight direction. The resulting pencil beams are integrated in the parameterized outdoor scenario we describe in the next paragraph. Using the shooting and bouncing rays (SBR+) solver[1], the channel is determined in frequency domain: We use $f_0 = 26.5\,\text{GHz}$ (band n257) with 400 MHz bandwidth and 0 dBm transmit power. Considering 60 kHz subcarrier spacing (SCS) numerology and frequency domain channel state information reference signal (CSI-RS) density of 1, the channel is simulated for $N = 555$ frequency bins with $\Delta f = 720\,\text{kHz}$ spacing.

The considered mmWave deployment is depicted in Fig. 2a, in which a BS (height: 10 m) serves a mounted UE (height: 4 m) to provide FWA (horizontal distance: 10 m), e.g. to a suburban house or to an industrial facility building in range of a private campus network deployment. However, in this environment there is not just one distinct link opportunity between the two network nodes as there is opportune multipath, i.e. the *ground reflection* (GR) and two *building reflections* {*1, 2*} (BR1, BR2), as shown in Fig. 2b–2d. Both buildings are 15 m away from BS and UE, respectively.

In the upper part of Tab. I we provide the respective ideal UE-side beam orientations in azimuth (ϕ) and elevation (θ) domain as well as the resulting received signal strength (RSS) of the directional channels. The lower part of Tab. I provides similar information for the LOS paths of UEs {2, 3, 4}, see Fig. 3. This second *multi-UE M^{3}S* setup (1 m spacings) will be used for a brief comparison with this work's *multipath-enabled M^{3}S* setup. The possible path combination and accompanying *condition number of matrix A (CN(A))* are provided in Tab. II.

For this scenario, an infrastructure monitoring case study assesses the enhanced technique's capability to monitor critical infrastructure for small-scale motions, e.g. to detect earthquakes (Trajs. 1-2) or subsidence processes in mining regions (Traj. 3), among others as described in [5], with one UE. We therefore investigate three sample trajectories affecting both infrastructure and mounted UE as illustrated in Fig. 4. The infrastructure self-motions $\overrightarrow{m_{\text{move}}}$ thus have a magnitude of up to 5 mm and the form of a scaled normal basis column vector.

B. Evaluation Methodology

The evaluation first verifies the proposed technique enhancement functionality in Sec. IV-A. For this purpose, the reconstructed 3D motion $\overrightarrow{m_{\text{meas}}}$ is compared to the underlying simulated motion $\overrightarrow{m_{\text{move}}}$, which is one of the previously described three trajectories. Subsequently, a collation with the measurement accuracy of the replaced multipath-enabled M^{3}S is undertaken using the incurred *Euclidean 3D error*, for the case that both techniques leverage four available propagation paths. This is further supplemented by a take on *best effort* service performance, i.e. where less than available paths are used ($U = 3$). Last, we briefly investigate the impact of multipath propagation by further simulations facilitating 16×16 UPAs with 32.15 dBi gain and 2.94° HPBW.

The second part of our evaluation, cf. Sec. IV-B, conducts the first assessment of expectable real-world performance levels by considering typical sources of error. These are imposed on the simulated channels of the trajectories: first for y_{shift} (Traj. 2, high multipath), then for z_{shift} (Traj. 3, low multipath). The impact of each source of error is studied independently by looking at the arising distributions of movement estimation error based on 10,000 iterations per trajectory. For a fair assessment of the impact of each source of error for different $\|\overrightarrow{m_{\text{move}}}\|_2$, we consider the *$\overrightarrow{m_{move}}$-normalized 3D error* $1\,\text{mm} \cdot \|\overrightarrow{m_{\text{meas}}} - \overrightarrow{m_{\text{move}}}\|_2 / \|\overrightarrow{m_{\text{move}}}\|_2$, which is essentially a unit-affiliated relative error (RE).

C. Modeling of Considered Error Sources

Channel noise is considered via predetermined SNR thresholds. There are, however, two cases: Either the SNR is set

[1]Ansys Inc. High frequency simulation software (HFSS). [Online]. Available: www.ansys.com/hfss (Accessed 2022-09-12).

TABLE I
UE-SIDE PARAMETERS OF LEVERAGED PROPAGATION PATHS WITH AZ. AND EL. ANGLES (ϕ, θ) FOLLOWING CONVENTION IN FIG. 4D.

UE	Spatial Link Opportunity	ϕ [°]	θ [°]	RSS [dBm]
1	Line-of-Sight (LOS)	0.00	30.96	−42.72
1	Ground Reflection (GR)	0.00	−54.46	−55.78
1	Building Reflection 1 (BR1)	71.57	10.74	−63.67
1	Building Reflection 2 (BR2)	−71.57	10.74	−62.76
2	LOS	0.00	26.57	−42.36
3	LOS	5.71	30.84	−42.76
4	LOS	5.71	26.45	−42.40

TABLE II
COMBINATIONS OF AVAILABLE PATHS FOR SENSING INCL. BEST EFFORT SERVICE ASSESSMENT: SUITABILITY (✓) OR EXCLUSION (✗) BASED ON CHECK FOR LARGE CONDITION NUMBER (CN), CF. SEC. II-B.

Multipath-enabled M^{3}S		Multi-UE-based M^{3}S	
Used Paths (UE 1)	CN [dB]	Used UEs (LOS)	CN [dB]
{LOS, GR, BR1, BR2}	5.74	{1, 2, 3, 4}	16.97
{LOS, GR, BR1} ✓	4.58	{1, 2, 3} ✓	15.92
{LOS, GR, BR2} ✓	4.58	{1, 2, 4} ✓	17.56
{LOS, BR1, BR2} ✗	164.46	{1, 3, 4} ✓	17.99
{GR, BR1, BR2} ✓	7.56	{2, 3, 4} ✓	17.79

for the LOS path such that the SNRs of the other paths depends on the RSS difference, cf. Tab. I, or the SNR of all paths is set identically. Second, *beam misalignment* Δ_{BMA} is modeled by a truncated zero-mean Gaussian distribution [12] with std. dev. σ_{BMA}. The corresponding azimuth and elevation offsets $(\Delta\phi, \Delta\theta)$ are selected uniformly from the circular path $|\Delta_{BMA}|^2 = |\Delta\phi|^2 + |\Delta\theta|^2$. As lower and upper bounds of misalignment we use $\pm$HPBW/2 ($\approx 6.6\,°$) as a consequence of using the optimal exhaustive search algorithm with HPBW-spaced beam codebooks. In one case, we tighten the bounds to $\pm\sigma_{BMA}$ to consider excessive beam refinement. LOs suffer from random walks over time with a step size best described as a zero mean Gaussian random variable, hence, we model LO *phase noise* with step size variance σ^2_{PN} between consecutive measurements [13]. Analogue, we model the *sampling rate offsets* by $\mathcal{N}(0, \sigma_{SRO})$ in parts per million (ppm).

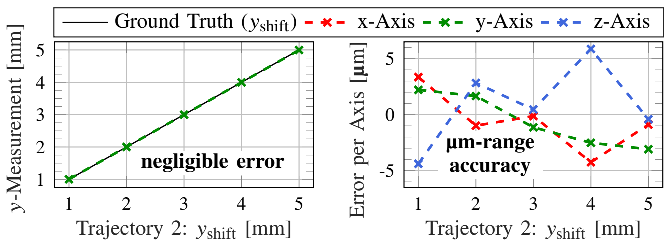

Fig. 5. Measuring Traj. 2 with UE 1's four propagation paths. The multipath-based single UE approach enables high-accuracy 3D tracking of fine motions, what was to be shown. Note the change of scale from mm (left) to µm (right).

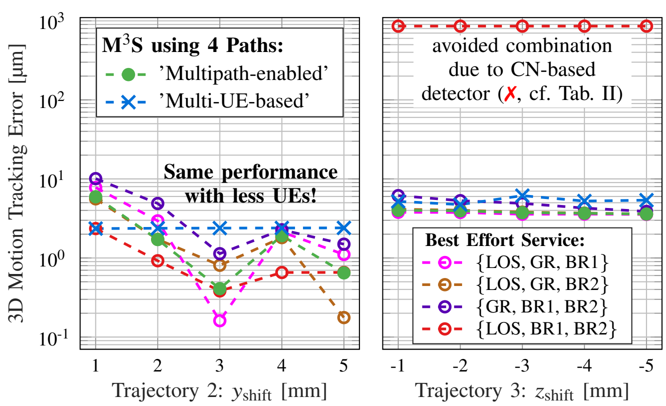

Fig. 6. Comparison of the two M^{3}S flavors, each using four propagation paths, yields similar performance as illustrated for Trajectories 2 and 3. Best effort services using three selected paths may offer a similar QoE.

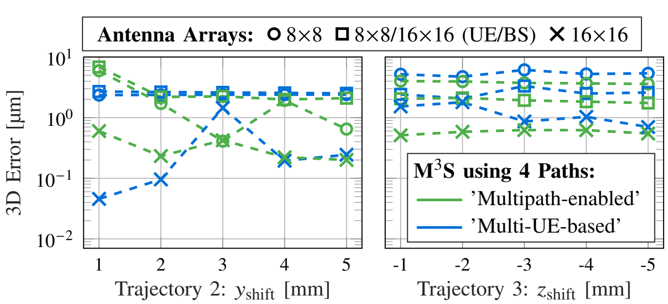

Fig. 7. Performance for different antenna arrays shows that undesired multipath components are mitigated by increased antenna directionality, yet no fixed gains are observed.

IV. Case Study: Infrastructure Monitoring

A. *Verification of New Multipath-Enabled M^{3}S Approach & Performance Comparison with Multi-UE-based M^{3}S*

Fig. 5 shows the results for the proposed multipath-enabled tracking approach for Traj. 2. On the left, one can see that the y-component of m_{meas} matches the true movement y_{shift}. On the right side the differences of movement components show that the individual errors are in the µm-range which is compliant with, for example, industry requirements for measuring of machine vibrations [7]. *This confirms that a single mounted UE is capable of measuring its own 3D motion with high accuracy in a sufficiently rich multipath environment.*

By means of Fig. 6 we further compare the measurement accuracy of the new technique to the multi-UE-based flavor for Trajs. 2-3[2]. It can be seen that, on average, the proposed technique does perform better. *We thus find that reducing the number of UEs by leveraging available multipath opportunities does not come at the cost of reduced performance.* Both schemes do not exceed the 10 µm error bound observed in [5]. As further illustrated this even leaves headroom for best effort services using the bare minimum number of paths ($U = 3$) as long as the used subset of paths is sensible based on condition number check, cf. checkmarks (✓) in Tab. II.

Investigation of Multipath Effects: It can be noticed in Fig. 6 that the performance of Traj. 2 differs drastically in the range from 10 µm to 0.2 µm. On average, leveraging all four paths incurs a RE of 1.4 µm for Traj. 2 compared to only 3.8 µm for the more stable estimates along Traj. 3. Considering footnote 2, the observed jitter for Traj. 2 indicates that either matrix A or undesired multipath bias the performance depending on movement vector $\overrightarrow{m_{\text{move}}}$. By adding the ideal expected phase shifts of the corresponding movements to the ray-tracing data for the baseline UE position, we test for the latter case: We find that the achieved performance for Traj. 2 stabilizes compared to Fig. 6. Additionally, the measurement accuracy further improves by several orders of magnitude. *This shows that multipath fluctuations along the infrastructure-mounted UE's motion induce measurement errors if they are strong enough; the fundamental presence of multipath components also sets the best-case accuracy level.*

By simulations employing UPAs with higher directionality we verify these observations. Fig. 7 shows the incurred 3D tracking error for both sensing techniques (with $U = 4$) for three UE-BS antenna array combinations. Our first observation is that the use of more directional arrays increases the likelihood for enhanced measurement accuracy, yet the performance gains vary significantly depending on the trajectory. This is compatible with our previous findings on the impact of multipath. On a further note, these results again do not support the hypothesis that the use of either of the two setups is generally superior to the other. While a strategic deployment of several UEs could indeed have its merits, multipath-enabled M^{3}S nonetheless offers a more practical alternative with high accuracy, if the radio environment allows for it.

[2] Results for Traj. 1 (along x-axis) not depicted due to similarities to Traj. 3.

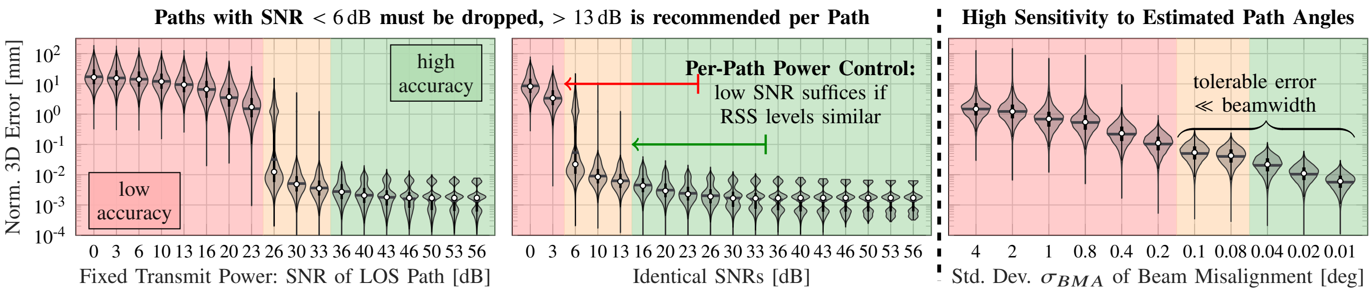

Fig. 8. Normalized Euclidean measurement error for Traj. 2 considering noise and beam misalignment.

B. Error Analysis for Multipath-Enabled Technique Considering Different Trajectories

1) Trajectory 2 (along y-axis, high multipath): The impact of AWGN is investigated twofold: *(1)* On the left side of Fig. 8 the distribution of incurred error over are depicted for different SNRs. It can be seen for SNRs smaller than 26 dB that the incurred error is usually as large as the underlying motion (≈ 1 mm). For SNRs between 26 to 33 dB the error is in the typical range but prone to occasional outliers. Several measurements of CSI-RS will be required in this region. For SNR ≥ 36 dB the mean loss in normalized error is less than 2.9 dB with the worst-case loss being 12.9 dB. This means that AWGN doubles the error when in high SNR conditions, whereas the maximum error may be up to 20 larger. Hence, there is a need for measurement aggregation depending on the available SNR. *(2)* The plot in the middle of Fig. 8 investigates the performance for all paths offering the same SNR. As a result, the previously discussed ranges of SNR are shifted by about 20 dB corresponding to the difference in RSS between strongest (LOS) and weakest BR1) leveraged link opportunities, cf. Tab. I. *This shows that high accuracy necessitates a per-path power control. When the transmit power cannot be increased further for a given path, but the SNR is insufficiently low, e.g. smaller than 6 dB, such propagation path must be dropped. Hence, the selection of suitable combinations of paths depends on both achievable SNRs and accompanying CN.*

On the right side of Fig. 8, we show the error distributions for different beam misalignments. Compared to the influence of noise the losses are more gradual. Further, it can easily be seen that *well-aligned beams are crucial* because the measurement error is often the size of the underlying movement if $\sigma_{BMA} \geq 0.2\,^{\circ}$. σ_{BMA} should not exceed $0.1\,^{\circ}$ for a reasonable measurement service quality. This requirement will prolong and complicate system setup, but may be achieved considering the Cramér-Rao orientation error bound (OEB)-based achievable std. dev. $\ll 0.1\,^{\circ}$ [14].

Further, we review the impact of oscillator imperfections, as shown in Fig. 9, which are mutually similar and also share these similarities with the previously discussed distributions within the high SNR regime. As low SNR and strong beam misalignments have a much greater impact on the 3D small-scale motion tracking service quality, we will not investigate LO imperfections in more depth.

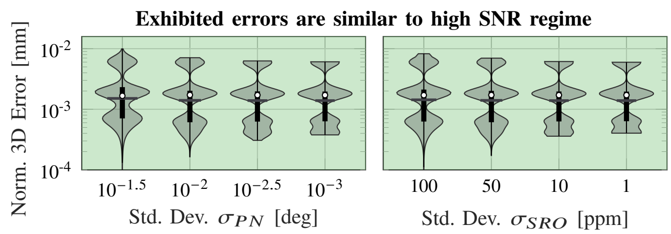

Fig. 9. Normalized 3D tracking error for Traj. 2 for typical phase noise (left) and sampling rate offsets (right).

We have also evaluated the error distributions for best effort services, e.g. for path combination {LOS, GR, BR1}: Not considering any additional errors, the average accuracy with $U = 3$ drops by 0.5 dB. Considering beam misalignments the mean loss increases proportionally (by 0.5-0.7 dB) compared to the $U = 4$ case. However, the mean losses due to AWGN and LO imperfections increase disproportionally (0.9-1.1 dB). This implies that best effort services may be less robust to channel phase distortions such as AWGN, phase noise, and sampling rate offsets.

2) Trajectory 3 (along neg. z-axis, low multipath): In comparison to the previous section we consider the impact of error sources on Traj. 3 which exhibits low multipath. Fig. 10 illustrates the distributions of normalized 3D error: The AWGN-based error (left) is now more compact with significantly reduced mean and maximum accuracy degradations. The tolerance for lower SNRs is also increased as emphasized by the change of background color coding. Hence, for such conditions, measurement aggregation may only be required for additional robustness where SNR ≤ 10 dB. As before, LO imperfections (not depicted) degrade performance similar to the AWGN-based distributions with SNR ≥ 36 dB. We note that this clear difference in performance between Trajs. 2-3 is also observed for Trajs. 1-2. *Referring back to Sec. IV-A, this shows that multipath previously amplified the errors due to AWGN and LO.* This is supported by the minuscule change of impact from erroneous angles, cf. right side of Fig. 10. *Beam misalignments therefore remain a multipath-independent source of error.*

As observed in [15], misalignments of a few degrees can already deteriorate the data rate by several hundred Mbps. In order to minimize these losses, or when providing angle-assisted UE positioning services [9], mmWave networks will take additional measures such that the previous assumption of ±HPBW/2 misalignment bounds is pessimistic. We therefore

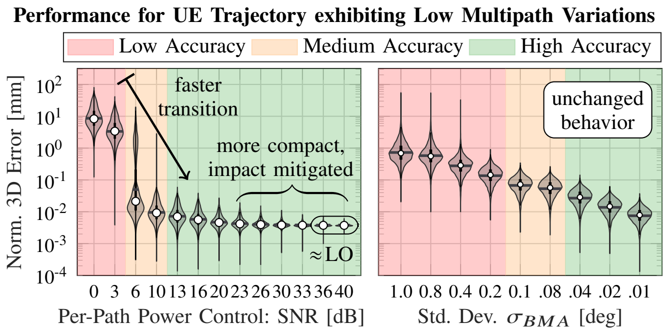

Fig. 10. Tracking performance under AWGN and beam misalignment for Trajectory 3: Gradually sinking house (subsidence process) can be measured with high accuracy. Annotations make comparison to Traj. 2 results (Fig. 8) where there are stronger multipath variations.

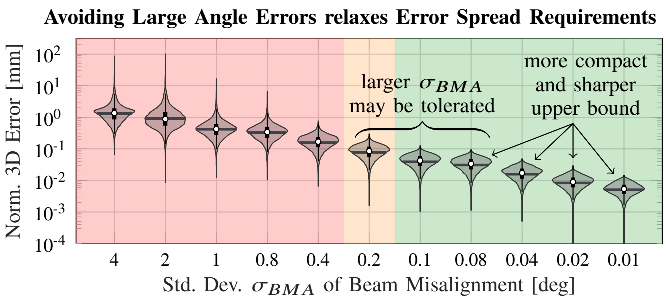

Fig. 11. Incurred errors for $\pm\sigma_{BMA}$-bounded beam misalignment compared to $\pm$HPBW/2 bounds (Fig. 10).

revisit beam misalignment-based measurements errors with tightened bounds $\pm\sigma_{BMA}$ of the truncated Gaussian distribution. The resulting performance distributions are shown in Fig. 11. Comparing these to Fig. 10, we find that the mean performance degradation is reduced by about 1.7-2.3 dB for $\sigma_{BMA} \leq 0.2^\circ$, with worst case errors being cut by up to 4.9 dB. As the change in background color coding between the two plots indicates, tighter bounds increase tolerance for larger σ_{BMA}. *While this shows that use of angle estimation algorithms with tight error bounds is certainly helpful, it is yet reaffirmed that M^{3}S primarily requires algorithms with low std. dev. ($\sigma_{BMA} \leq 0.1^\circ$) to enable high-accuracy tracking.*

V. Summary

This work has enhanced the *mmWave microscopic 3D motion sensing (M^{3}S)* technique efficiency, thereby allowing for tracking of fine-grained 3D motions with sub-10 µm accuracy by exploiting distinct mmWave channels between the BS and UE. Based on 3D ray-tracing simulation data, we have demonstrated that the new *multipath-based* design offers a similar service quality as the conventional multi-UE-based flavor. While this technique is restricted to environments with reasonable multipath richness, e.g. urban regions, we have nevertheless showed that the applicability is increased at no sacrifice in performance. Moreover, a lack of spatial link opportunities may still be made up by using links to several BSs or by deploying reconfigurable intelligent surfaces (RISs).

Our performance investigation under realistic impairments has yielded the following results. Beyond the need for at least three propagation paths, per-path power control must be used to serve sufficient SNR for high accuracy ($\geq$ 13 dB). In the worst case available paths must be omitted (< 6 dB), but we showed that such best effort services are nonetheless feasible. Local oscillator (LO) imperfections induce errors similar to the operation in high SNR regimes. While noise and LO effects are bearable, their impact is particularly emphasized if the multipath components fluctuate strongly throughout the UE's movement. Larger antenna arrays can reduce this disadvantage of multipath propagation although no fixed gain is observed. Future work could therefore investigate the benefits of suppressing key interfering paths using customized beam patterns. Finally, we have determined that minimizing beam misalignment errors such that $\sigma_{BMA} < 0.2^\circ$ will be critical for any M^{3}S deployment to ensure the functionality of the 3D tracking algorithm. In our next work, we will therefore evaluate angle estimation algorithms with our mmWave platform [9].

Acknowledgment

This work has been partly funded by the German Federal Ministry of Education and Research (BMBF) in the course of the *6GEM Research Hub* under grant number 16KISK038, by the German Research Foundation (DFG) within the *Collaborative Research Center SFB 876* "Providing Information by Resource-Constrained Analysis," project A4, as well as by the Ministry of Economic Affairs, Industry, Climate Protection and Energy of the State of North Rhine-Westphalia (MWIKE NRW) along with the *Competence Center 5G.NRW* under grant number 005-01903-0047.

References

[1] J. A. Zhang *et al.*, "Enabling joint communication and radar sensing in mobile networks - a survey," *IEEE Commun. Surv. & Tutor.*, Mar. 2022.

[2] M. Xiao *et al.*, "Millimeter wave communications for future mobile networks," *IEEE J. Sel. Areas Commun.*, vol. 35, no. 9, Sep. 2017.

[3] S. Rangan, T. S. Rappaport, and E. Erkip, "Millimeter-wave cellular wireless networks: Potentials and challenges," *Proc. of the IEEE*, vol. 102, no. 3, Mar. 2014.

[4] B. Sliwa, N. Piatkowski, and C.Wietfeld, "The channel as a traffic sensor: Vehicle detection and classification based on radio fingerprinting," *IEEE Internet of Things Journal*, vol. 7, no. 8, Mar. 2020.

[5] S. Häger, S. Böcker, S. Jamali, T. Reinsch, and C. Wietfeld, "A novel system architecture for small-scale motion sensing exploiting 5G mmWave channels," in *IEEE GLOBECOM Workshops*, Dec. 2021.

[6] China Academy of Telecom. Tech. (CATT), "3GPP R1-1810532: Discussion of potential techniques for NR positioning," Oct. 2018.

[7] C. Jiang *et al.*, "mmVib: Micrometer-level vibration measurement with mmWave radar," in *Proc. 26th ACM Annu. Int. Conf. on Mobile Computing and Networking (MobiCom)*, no. 45, Sep. 2020.

[8] L. Wei, Q. Li, and G. Wu, "Exhaustive, iterative and hybrid initial access techniques in mmWave communications," in *IEEE Wireless Communications and Networking Conf. (WCNC)*, Mar. 2017.

[9] K. Heimann, J. Tiemann, S. Böcker, and C. Wietfeld, "Cross–bearing based positioning as a feature of 5G millimeter wave beam alignment," in *IEEE Vehicular Technology Conf. (VTC-Spring)*, May 2020.

[10] A. Ichkov *et al.*, "Empirical study of mobility support in millimeter-wave outdoor urban deployments," in *IEEE Int. Conf. on Communications (ICC)*, Jun. 2021.

[11] K. Heimann, B. Sliwa, M. Patchou, and C. Wietfeld, "Modeling and simulation of reconfigurable intelligent surfaces for hybrid aerial and ground-based vehicular communications," in *Int. ACM Conf. on Modeling, Anal. and Simul. of Wirel. and Mob. Sys. (MSWiM)*, Nov. 2021.

[12] A. Thornburg and R. W. Heath, "Ergodic capacity in mmWave ad hoc network with imperfect beam alignment," in *IEEE Military Communications Conf. (MILCOM)*, Oct. 2015.

[13] F. Munier *et al.*, "Estimation of phase noise for QPSK modulation over AWGN channels," in *Proc. GigaHertz 2003 Symp.*, Nov. 2003.

[14] A. Guerra, F. Guidi, and D. Dardari, "Position and orientation error bound for wideband massive antenna arrays," in *IEEE Int. Conf. on Communications Workshops (ICC Wkshps)*, Jun. 2015.

[15] K. Heimann, J. Tiemann, S. Böcker, and C. Wietfeld, "On the potential of 5G mmWave pencil beam antennas for UAV communications: An experimental evaluation," in *ITG Wkshp. on Smart Antennas (WSA)*, Mar. 2018.